
Towards Coordinate- and Dimension-Agnostic Machine Learning for Partial Differential Equations

Trung V. Phan

Department of Chemical and Biomolecular Engineering
Johns Hopkins University
Baltimore, MD 21218
tphan23@jhu.edu

George A. Kevrekidis

Department of Applied Mathematics and Statistics
Johns Hopkins University
Baltimore, MD 21218
gkevrek1@jhu.edu

Soledad Villar

Department of Applied Mathematics and Statistics
Johns Hopkins University
Baltimore, MD 21218
svillar3@jhu.edu

Yannis G. Kevrekidis

Department of Applied Mathematics and Statistics
Johns Hopkins University
Baltimore, MD 21218
yannisk@jhu.edu

Juan M. Bello-Rivas *†

Department of Chemical and Biomolecular Engineering
Johns Hopkins University
Baltimore, MD 21218
jmbr@superadditive.com

Abstract

The machine learning methods for data-driven identification of partial differential equations (PDEs) are typically defined for a given number of spatial dimensions and a choice of coordinates the data have been collected in. This dependence prevents the learned evolution equation from generalizing to other spaces. In this work, we reformulate the problem in terms of *coordinate-* and *dimension-independent* representations, paving the way toward what we call “spatially liberated” PDE learning. To this end, we employ a machine learning approach to predict the evolution of scalar field systems expressed in the formalism of exterior calculus, which is *coordinate-free* and immediately generalizes to arbitrary dimensions by construction. We demonstrate the performance of this approach in the FitzHugh-

*Current address: Microsoft Azure Quantum

†Corresponding author

Nagumo and Barkley reaction-diffusion models, as well as the Patlak-Keller-Segel model informed by *in-situ* chemotactic bacteria observations. We provide extensive numerical experiments that demonstrate that our approach allows for seamless transitions across various spatial contexts. We show that the field dynamics learned in one space can be used to make accurate predictions in other spaces with different dimensions, coordinate systems, boundary conditions, and curvatures.

1 Introduction

Machine learning has traditionally been used to identify and model partial differential equations (PDEs) from observational data [32, 20, 5, 11]. In particular, deep learning techniques such as physics-informed machine learning [27, 52] and operator learning [36, 31, 16], often in combination with symbolic regression techniques [6, 10], can extract spatiotemporal patterns from experimental measurements and (approximately) learn the underlying physical laws. This has been especially useful for describing complex dynamical systems in various scientific and engineering domains, where conventional numerical methods can be computationally expensive [29], or where we only have access to an incomplete description of the system [38]. As a result, machine learning based modeling of PDEs is used on a wide range of scales, from fine-grained descriptions at the particle level [33] to coarse-grained representations in terms of density fields [51], providing a data-driven alternative to traditional physics-based derivations.

Real-world data are often expressed in domains and coordinate systems that are determined by the experimental acquisition process. For instance, bacterial chemotaxis can be captured as one-dimensional wave channels [2], or visualized as two-dimensional images — top-down with upright [50] or bottom-up with inverted microscopy [42]. All three experimental settings produce data of the same physical process supported in different geometries and coordinate systems. The conventional machine learning approaches for PDE identification are inherently tied to a predefined spatial framework, preventing them from generalizing the learned physical mechanism to different coordinate systems, geometries, or dimensions. In this work we propose a more flexible approach that would allow learning a dynamical system (a physical mechanistic model) from data in one domain, and then making accurate predictions in another, when the underlying physics is the same. Recent work by Psarellis et al. [51] has proposed a coordinate-free PDE learning approach using exterior calculus. Their method allows them to learn a PDE independently of the coordinate system, and they show that the learning generalizes to different coordinate system representations of the same domain. We further extend the method to generalize to other domains with different geometries and dimensions.

Our contributions

Inspired by the work by Psarellis et al. [51], we propose a machine learning approach that can learn a PDE in one domain and generalize it to different domains and dimensions. Our approach applies to PDEs that describe the evolution of multiple coupled scalar fields. We only consider PDE operators that are invariant with respect to local orthogonal symmetries [59, 19, 43, 1, 57], which is a feature observed in many natural phenomena. For these systems, we show how machine learning can achieve “full spatial liberation,” enabling training in any space and coordinate system, yet being able to make accurate predictions across all others, regardless of coordinates, but also dimensions, boundary conditions, and spatial *intrinsic* curvatures (i.e. non-vanishing Riemann curvature tensor [15]). Fusion of training data obtained at different coordinates/geometries is also enabled.

In our experiments, we use neural networks to identify the FitzHugh-Nagumo [3] and Barkley [4] reaction-diffusion model operators; and a modified Patlak-Keller-Segel model, derived from *in-situ* observations of chemotactic bacteria [50]. We train the models on data generated in a periodic one-dimensional space using Cartesian coordinates, and then demonstrate their ability to generalize to higher-dimensional spaces. These include two- and three-dimensional Euclidean spaces in Cartesian or non-Cartesian coordinates, as well as a two-dimensional submanifold of a sphere in Euclidean space, described using geographic as well as stereographic coordinates. We also consider different boundary conditions in these new spaces, such as a no-flux Neumann boundary.

2 Coordinate-free Operator Learning Across Dimensions

For most³ differential equations defined on a Riemannian manifold \mathcal{M} with metric g , there exists a coordinate-free mathematical expression that represents them as an exterior differential system (EDS) [7, 41], in terms of differential forms on \mathcal{M} . We describe the language of differential forms and give references in Appendix A. Given an EDS, one can express a particular PDE in coordinate-explicit form after choosing a coordinate system on the manifold \mathcal{M} , and transformations of the PDE under diffeomorphisms of \mathcal{M} are governed by the chain rule (pullbacks). Certain EDSs exhibit *additional structure* that allows us to define them on spaces of varying dimension; we give the following simple example:

Example. *The heat equation of a scalar temperature field can be expressed in a coordinate-free way using differential forms as*

$$\frac{\partial u}{\partial t} = \star d \star du, \quad (1)$$

where d is the exterior derivative and \star is the Hodge star operator.

In addition to being coordinate-free, the heat equation in equation (1) is “domain-agnostic” and “dimension-agnostic” — meaning that the same heat equation can be defined on any manifold \mathcal{M} of any dimension. The dimension and the Riemannian metric appear via the definitions of d and \star . In this paper we argue that we can learn the right hand side of an evolution equation in one domain and transfer its learning to other manifolds of different dimensions, as long as the differential equation is defined as a “dimension-agnostic” expression.

Many PDEs of mathematical physics and other fields of science and engineering can be expressed in a coordinate-free manner in terms of their independent variables and their (unknown) fields. Notable examples are the Navier-Stokes [60] equations and, more generally, the equations of continuum mechanics [37], the Fokker-Planck equation [40], the Kuramoto-Sivashinsky equation [18], as well as many others.

Our work in this paper focuses exclusively on systems of scalar fields (0-forms) governed by PDEs invariant under local orthogonal transformations (rotations and reflections) and under diffeomorphic translations [19, 43, 1]. Such systems arise frequently in nature, as microscopic physical interactions typically exhibit these symmetries; thus, the emergent PDEs inherit them at macroscopic scales. We consider the PDE to involve at most second-order⁴ spatial-derivatives, in which we adopt the power-counting scheme of effective field theory [25, 9] with the total differential order of each term defined as the sum of its derivative orders.⁵ We then observe that when we apply these restrictions, the resulting class of PDEs turn out to be domain-free and dimension-free and we can therefore generalize the learning to other domains in other dimensions.

Our approach can be summarized in two main steps (see Figure 1):

1. Given data satisfying an evolution equation, first learn a spatially coordinate-free representation of the evolution operator of the PDE expressed in terms of differential forms,
2. Given a new set of initial and/or boundary conditions in a possibly different coordinate system, or even dimension, use a coordinate-free solution of the PDE to evolve the dynamics.

Note that coordinate-free integrators are a classical subject of study in numerical analysis [14].

Generators of invariant 0-forms. Given N scalar fields $\{\Psi_1, \dots, \Psi_N\}$ (i.e. 0-forms in a Riemannian manifold \mathcal{M}) the set of all possible orthogonally symmetric operators from 0-forms to 0-forms involving up to second-order derivatives can be obtained from:

- The Laplacians:

$$\star d \star d\Psi_j, \quad (2)$$

³For a precise statement see page 4 of [8].

⁴Higher-order will be considered in future works by extending the invariant features discussed in Eq. (5).

⁵This is the power-counting scheme for wave numbers, which is of critical importance when creating an effective field theory for coarse-grained dynamics [25, 9]. Since each spatial derivative introduces a factor of the wave number (e.g. in Fourier space), higher-order terms are increasingly suppressed at low wave numbers. By explicitly tracking the total derivative order, this method provides a more accurate characterization of the dominant large-scale emergent behavior of the system.

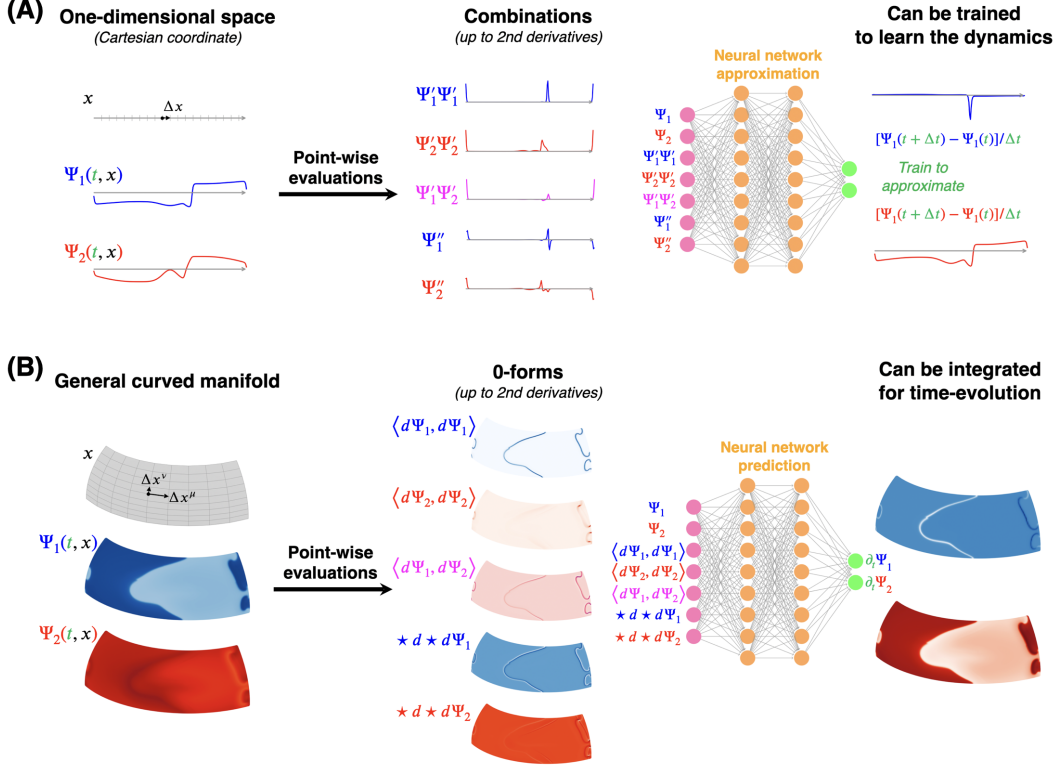


Figure 1: We aim to demonstrate that it is possible to identify a class of evolutionary PDE systems in a coordinate- and dimension-free manner using neural networks. We package the input in a coordinate- and dimension-free manner. **(A)** We learn the one-dimensional space right-hand-side operator of the PDEs in a Cartesian coordinate. **(B)** We can then simulate the dynamics in arbitrary coordinates and dimensions (the figure illustrates the case of two-dimensional curved space).

where $j = 1, \dots, N$. There are N of them in total.

- The inner products:

$$\langle d\Psi_j, d\Psi_k \rangle \equiv \star (d\Psi_j \wedge \star d\Psi_k), \quad (3)$$

where $j, k = 1, \dots, N$. Since these are symmetric, there are $N(N + 1)/2$ distinct products.

In the above expressions, *the Hodge star* \star maps k -forms to $(n - k)$ -forms where n is the dimension of the space. The Laplacians in (2) and the inner products in (3) are with respect to the Riemannian metric of \mathcal{M} . These operators can be written explicitly in coordinates using the metric structure of the manifold (see Appendix A).

Coordinate-free learning. Given Ψ_1, \dots, Ψ_N as above we consider the PDE identification problem

$$\frac{\partial \Psi_j}{\partial t} = \mathcal{F}_j(\Psi_1, \dots, \Psi_N, t), \quad j = 1, \dots, N \quad (4)$$

where we assume the \mathcal{F}_j 's are (possibly non-linear) orthogonally symmetric second order operators defining the right-hand-side of the evolutionary PDE. All second-order, functionally independent scalar invariants (0-forms), can be built from the original scalar fields, their gradient inner products, and their Laplacians, which follows from the first fundamental theorem of classical invariant theory for the orthogonal group [58, 54], which has been extensively used in machine learning [56, 21].⁶

⁶All $SO(n)$ -scalars can be built locally from derivatives of scalars, the metric (Kronecker delta), and the Levi-Civita symbol via basic arithmetic operations and contractions [54]; for $O(n)$ -invariance the Levi-Civita symbol is excluded. Our claim comes from applying this theorem to the second-order jet space, in which in this work we restrict to scalar expressions with total order of derivatives at most two. For higher-order, we can list all possible features constructed from the metric, the fields, and its derivatives — up to the desired order — to be used as invariant features.

Remark 1. Parity invariance under the full orthogonal group $O(n)$, which extends the rotational symmetries of $SO(n)$ to include reflections, excludes pseudoscalars. For instance, in dimension $n = 2$ it excludes the Jacobian determinant 0-form $\star(d\Psi_j \wedge d\Psi_k)$. Note that this expression does not define a 0-form in dimensions $n \neq 2$.

We construct the invariant features

$$\mathcal{B} = ([\Psi_j]_{j=1}^N, [\star d \star d\Psi_j]_{j=1}^N, [\langle d\Psi_j, d\Psi_k \rangle]_{1 \leq j < k \leq N}) =: (b_1, \dots, b_{\frac{N(N+5)}{2}}) \quad (5)$$

to use them as input features for neural networks $\hat{\mathcal{F}}_j(\mathcal{B})$ ($j = 1, \dots, N$) that learn the right-hand-sides of (4). Namely, it learns functions $\hat{\mathcal{F}}_j(\mathcal{B})$ such that the integration of the corresponding PDE via a coordinate-free integrator approximates the training data. A **coordinate-free integrator** in this context is one that performs the integration of the PDE in terms of the features b_i . Note that this approach can be seen as a form of canonicalization (see [24, 45]), where the input data is transformed into a set of canonical invariants (here \mathcal{B}) to perform the learning.

Any-dimensional coordinate-free learning. The Laplacians and inner products are defined as functions of the input scalar fields for any domain –any Riemannian manifold (\mathcal{M}, g) of any dimension n . Therefore \mathcal{B} is defined via a domain- and dimension-independent description. The $\hat{\mathcal{F}}_j$'s are defined as functions of $N(N+5)/2$ features, $(b_1, \dots, b_{N(N+5)/2})$, independently of the size of the domain of the b_i 's (and thus independently of the dimension of the domain of the input 0-forms Ψ_j 's). Therefore the $\hat{\mathcal{F}}_j$ can be used to predict the dynamics of a family of PDEs defined in any input space.

This principle, of using a fixed set of parameters to define models in spaces of any size, is common in machine learning. In particular, these ideas appear in equivariant machine learning, where models such as graph neural networks use a fixed set of parameters to define functions on input graphs of any size [53, 39, 55]. The idea in the context of this work is illustrated in Figure 1. The theoretical treatment of the topic in the context of machine learning is pioneered in recent work by Levin and Díaz [34], using tools from the field of representation stability [17].

3 Examples

In this work, we apply the proposed methodology to three PDEs that can be expressed in a coordinate-free and dimension-free form, each involving two coupled scalar fields (thus $N = 2$ in Eq. (4) and Eq. (5)).

3.1 The FitzHugh-Nagumo System

In the FitzHugh-Nagumo system [3] two scalar fields participate: the excitation variable $V(x, t)$ and the recovery variable $W(x, t)$. The spatiotemporal dynamics of these fields are governed by the set of two coupled PDEs:

$$\begin{aligned} \partial_t V(x, t) &= \vec{\nabla}^2 V(x, t) + V(x, t) - \frac{1}{3} V^3(x, t) - W(x, t), \\ \partial_t W(x, t) &= \varepsilon [V(x, t) + \beta - \gamma W(x, t)], \end{aligned} \quad (6)$$

where we set $(\varepsilon, \beta, \gamma) = (0.02, 0, 0.5)$. For this choice of parameters, the system generates spiral waves in two-dimensional space and scroll waves in three-dimensional space, whereas such phenomena do not emerge in dimension one. In coordinate-free form, the PDE can be expressed as:

$$\begin{aligned} \partial_t V(t) &= \star d \star dV(t) + V(t) - \frac{1}{3} V^3(t) - W(t), \\ \partial_t W(t) &= \varepsilon [V(t) + \beta - \gamma W(t)], \end{aligned} \quad (7)$$

where the location x can be omitted from the equation since this is a *spatial* coordinate-free formalism. For brevity, we express all PDEs from this point onward in coordinate-free representation.

3.2 The Barkley System

The Barkley reaction-diffusion system [4] models excitable media and oscillatory media. It is often used as a qualitative model in pattern forming systems like the Belousov-Zhabotinsky reaction and

other systems that are well described by the interaction of an activator and an inhibitor component. In the simplest case, the Barkley system is described by a set of two coupled PDEs:

$$\begin{aligned}\partial_t U(t) &= \star d \star dU(t) + \frac{1}{\varepsilon} U(t) [1 - U(t)] \left[U(t) - \frac{V(t) + b}{a} \right], \\ \partial_t V(t) &= U(t) - V(t),\end{aligned}\tag{8}$$

where we choose the parameters $(\varepsilon, a, b) = (0.02, 0.75, 0.02)$ so that this system can generate spiral and scroll waves in two- and three-dimensional spaces respectively. For a coordinate-explicit form of the equation, see Appendix C.

3.3 A Modified Patlak-Keller-Segel System

Recent technological advancements have enabled us to directly measure *in situ* the time-evolution dynamics of bacterial density and the concentration of environmental cues to which the bacteria respond, with high precision [49]. We can therefore develop much more accurate, macroscopic mathematical models to describe the collective behavior of bacterial swarms. We consider the *modified* Patlak-Keller-Segel model for bacterial chemotaxis as proposed in [49], supported by direct *in situ* observations of *E. coli* (*Escherichia coli*) density and Asp (Aspartate) chemoattractants. The dynamics are described by a set of two PDEs, which can be written in a non-dimensionalized form as follows:

$$\begin{aligned}\partial_t A(t) &= \star d \star dA(t) - \left[\frac{A(t)}{1 + A(t)} \right] \left[\frac{B(t)}{1 + B(t)} \right], \\ \partial_t B(t) &= \alpha B(t) + \star d \star d [D_B B(t)] - \star d \star d \{ \chi[B(t)] \Phi[A(t)] \},\end{aligned}\tag{9}$$

where the parameters are estimated from experiments to be $\alpha \approx 1.5 \times 10^{-4}$, $D_B \approx 0.55$, $\chi_0 \approx 4.8$, $B_h \approx 1.3$, and $K_i \approx 0.27$. The field $A(x, t)$ represents the chemical concentration, and the field $B(x, t)$ represents the bacterial density. The effective chemosensitivity is denoted by $\chi[B(t)]$ and the perceived chemical signal $\Phi[A(t)]$ is defined as:

$$\chi[B(t)] = \chi_0 \left[\frac{B(t)}{1 + B(t)/B_h} \right], \quad \Phi[A(t)] = \ln \left[1 + \frac{A(t)}{K_i} \right].\tag{10}$$

For a coordinate-explicit form of the equation, see Appendix C.

4 Computational Experiments

For each of the systems of Section 3 we follow the same workflow:

1. Given training data of the scalar fields $\{\Psi_i(x, t)\}_{i=0}^N$ in *one*-dimensional Euclidean space, we project the data onto the spatial coordinate-free basis \mathcal{B} of (5) and estimate the time derivatives $\{\partial \hat{\Psi}_i / \partial t\}$ using a finite-difference scheme,
2. We train a fully-connected neural network $\hat{\mathcal{F}}_{\text{NN}}$ to predict $\{\partial \hat{\Psi}_i / \partial t\}$ from the basis \mathcal{B} ,
3. Given the trained network $\hat{\mathcal{F}}_{\text{NN}}$, we integrate the corresponding scalar fields (now defined on different choices of domain) given initial conditions.

We provide numerical examples for the following domains:

1. Section 4.1: 1-Dimensional Euclidean Space (periodic boundary conditions) with Cartesian and non-Cartesian coordinates,
2. Section 4.2: 2-Dimensional Euclidean Space (periodic boundary conditions) with Cartesian and non-Cartesian coordinates, and 3-Dimensional Euclidean Space (Neumann no-flux boundary conditions) with Cartesian coordinates,
3. Section 4.3: 2-Dimensional intrinsically curved surface (heterogeneous boundary conditions) embedded in 3-Dimensional Euclidean Space with geographic and stereographic coordinates,

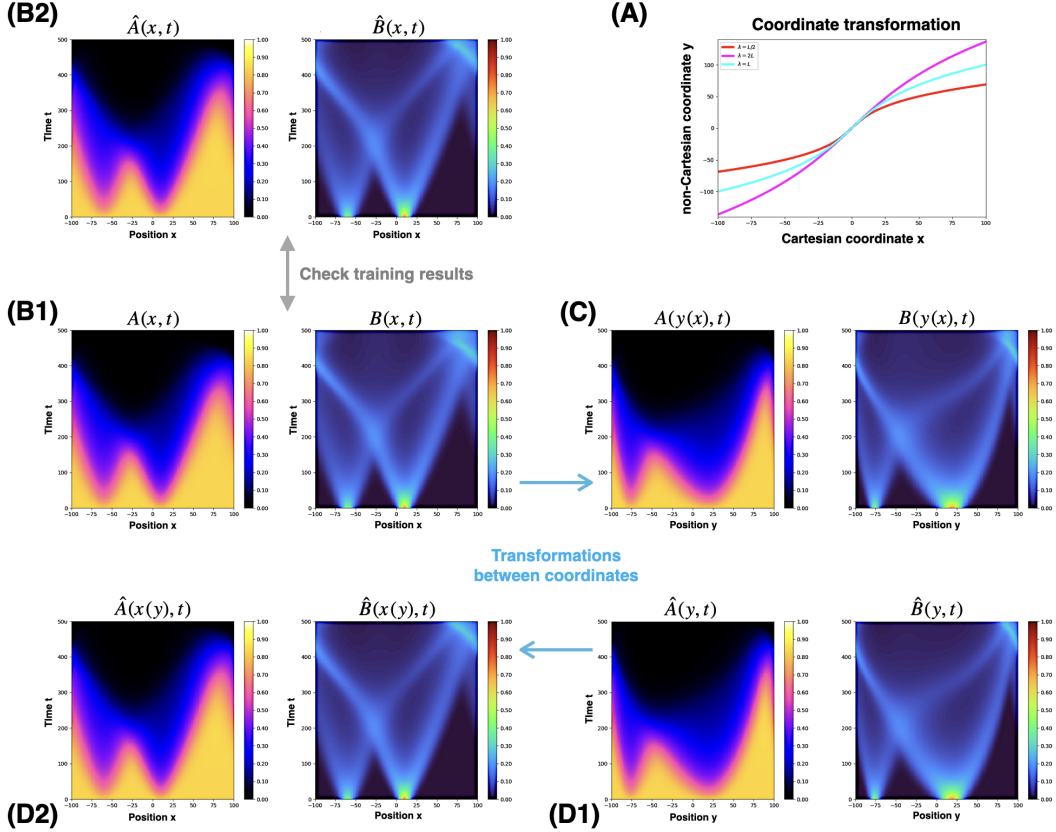


Figure 2: The Patlak-Keller-Segel field evolution dynamics in a periodic one-dimensional space, with different coordinate systems. The initial field configurations are the same, up to an extrapolation when transitioning between different coordinate systems. (A) The Cartesian and non-Cartesian coordinate systems, using Eq. (11) with different values of L to convert between x and y . (B1) The time progression of the fields when integrating Eq. (29) to generate the true dynamics Cartesian coordinate x . (B2) The time progression of the fields when using the trained neural network to generate the learned dynamics in the Cartesian coordinate x . (C) Transformation of Fig. (B1) into the non-Cartesian coordinate y . (D1) The time progression of the fields when using the trained neural network to generate the learned dynamics in the non-Cartesian coordinate y . (D2) Transformation of Fig. (D1) into the Cartesian coordinate x .

The learning of all PDE systems is conducted on data from a one-dimensional periodic domain $x \in [-L, +L]$. The data and neural network architectures are detailed in Appendix D. All simulations use evenly spaced grids for finite-difference computations in the specified coordinate system, and we verify that the numerical schemes are robust to space-time discretizations (see Appendix H). For notational convenience, we denote the fields obtained by numerically integrating the exact PDE as Ψ_i , and the predictions generated by the neural network models as $\hat{\Psi}_i$. The argument $\eta(\zeta)$ denotes that the computation was performed in ζ -coordinates and has been push-forwarded into η -coordinates via a coordinate transformation. A uniform grid in ζ -coordinates will in general correspond to a non-uniform grid in η -coordinates.

All quantitative comparisons between the “true” and learned dynamics are contained in Appendix J.

4.1 One-Dimensional Euclidean Space

In this example, we learn the Patlak-Keller-Segel field evolution dynamics in a periodic one-dimensional space. We train a network with data in 1-D Cartesian coordinates x , and we test its performance under a change of coordinates y in the same 1-D domain. Specifically y is related to x by the monotonic but nonlinear function:

$$x = f(y) \equiv x(y) = (y/2) [1 + (y/\lambda)^2] , \quad (11)$$

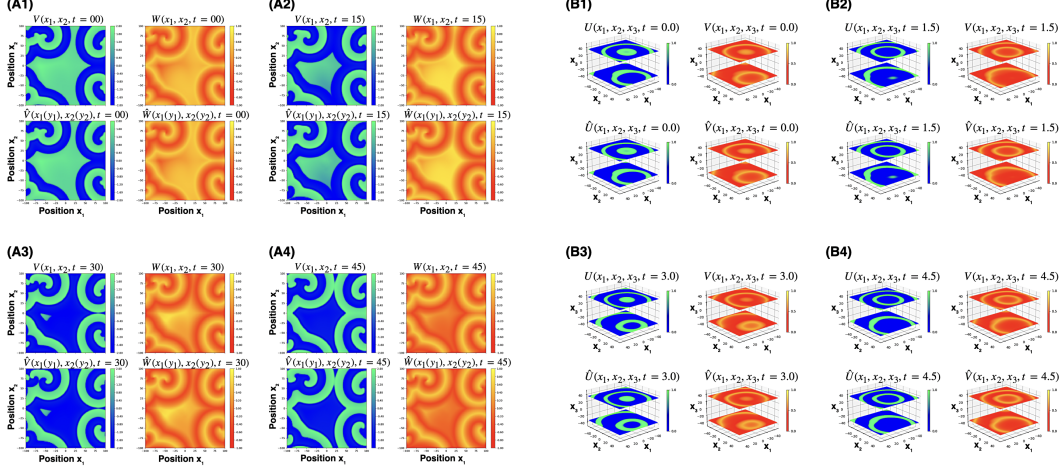


Figure 3: The time evolution dynamics of FitzHugh-Nagumo and Barkley systems in higher-dimensional Euclidean spaces. We study the FitzHugh-Nagumo system on a two-dimensional domain with periodic boundary conditions under various coordinate representations in (A), and investigate the Barkley system in three-dimensional space subject to Neumann (no-flux) boundary conditions in (B). For (A), we present the time evolution of the true dynamics obtained by integrating Eq. (6) and compare it with the dynamics generated using the learned model at four different time frames: (A1) $t = 0$, (A2) $t = 15$, (A3) $t = 30$, (A4) $t = 45$. Each time frame consists of four two-dimensional plots: the top row shows the true dynamics, while the bottom row displays the neural network predictions; the left column corresponds to V -field and the right column to W -field of the FitzHugh-Nagumo system. For (B), we present the time evolution of the true dynamics obtained by integrating Eq. (28) and compare it with the dynamics generated using the learned model at four different time frames: (B1) $t = 0$, (B2) $t = 1.5$, (B3) $t = 3.0$, (B4) $t = 4.5$. Every time frame consists of four three-dimensional plots (each illustrated with two x_3 -slices, located at $x_3 = \pm 35$): the top row shows the true dynamics, while the bottom row displays the neural network predictions; the left column corresponds to U -field and the right column to V -field of the Barkley system.

as illustrated in Fig.2A. We set $\lambda = L$. The inverse function $y = f^{-1}(x) \equiv y(x)$ is provided in Appendix F.1. The input pre-processing for the neural network (Fig. 1B, in y -coordinate) is detailed in Appendix F.2.

We test the trained model on a new initial condition $t = 0$ with uniform A and localized peaks in B (see Appendix H.1). The true dynamics, $A(x, t)$ and $B(x, t)$, are obtained by integrating Eq.(29) (Fig.2B1); the learned dynamics, $\hat{A}(x, t)$ and $\hat{B}(x, t)$, are generated by the neural network (Fig.2B2) are a good approximation. To test our coordinate-free generalization claims, we interpolate the initial field configurations to y -coordinates (see Appendix G), integrate the neural network model to get $\hat{A}(y, t)$ and $\hat{B}(y, t)$ (Fig.2D1), and then map the results back to x -space to arrive at $\hat{A}(x(y), t)$ and $\hat{B}(x(y), t)$ (Fig.2D2). We can also transform Fig. 1B1 to y -coordinates, obtaining $A(y(x), t)$ and $B(y(x), t)$ as shown in Fig. 2C. We observe that Fig. 2C and Fig. 2D1 agree, as well as Fig. 2A1 and Fig. 2D2, demonstrating that our machine learning method generalizes across coordinate systems.

4.2 Two- and Three-Dimensional Euclidean Space

In this section we consider the FitzHugh-Nagumo system and the Barkley system trained in 1-D cartesian data. We first add spatial-dimension to the FitzHugh-Nagumo system during test time. Using the trained models, we predict dynamics in both Cartesian (x_1, x_2) and non-Cartesian (y_1, y_2) coordinates, related by:

$$x_1 = f(y_1) \equiv x_1(y_1), \quad x_2 = f(y_2) \equiv x_2(y_2), \quad (12)$$

where f is as in Eq.(11) and we set $\lambda = L$. The domain is the square $(x_1, x_2) \in [-L, +L] \times [-L, +L]$ with periodic boundaries. An illustration of (y_1, y_2) versus (x_1, x_2) is in Appendix F.1; input pre-processing in (y_1, y_2) -coordinates for the neural network is detailed in Appendix F.3.

Spiral waves can emerge for certain instances of the FitzHugh-Nagumo system. We choose an initial field configuration at $t = 0$ where the spiral wave pattern is clearly visible (an explanation of how

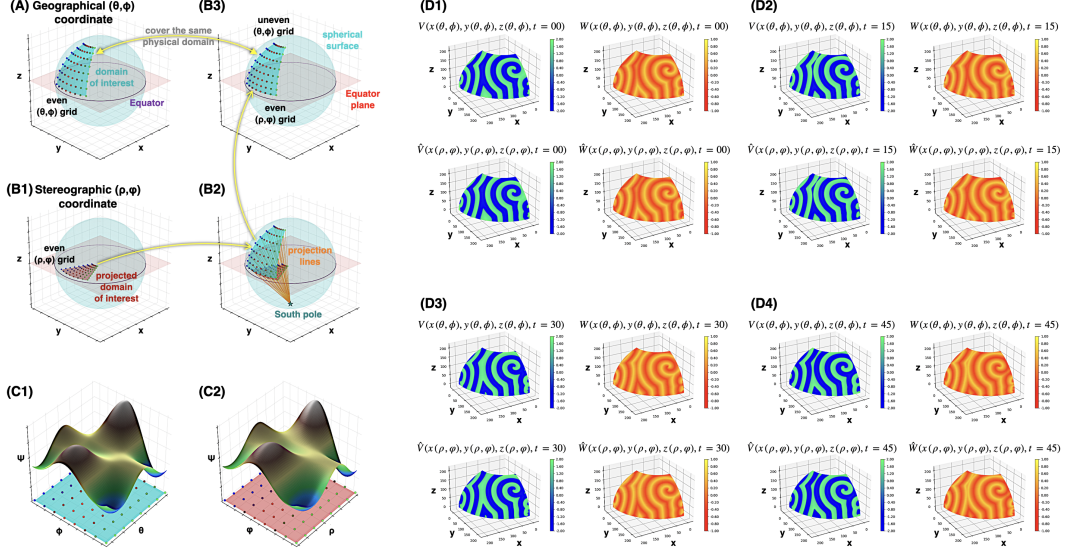


Figure 4: The time evolution of the FitzHugh–Nagumo system on a two-dimensional intrinsically curved surface. We illustrate the geographic and stereographic coordinate representations in (A–C), and in (D) compare the true dynamics obtained by integrating Eq. (7) in geographic coordinates with the learned dynamics generated in stereographic coordinates. In (A–B), we embed the spherical surface in three-dimensional Cartesian space (x, y, z) , showing the sphere in cyan, the equatorial plane in red, and their intersection—the equator—in purple: (A) shows a uniform grid in geographic coordinates (θ, ϕ) ; (B) shows a uniform grid in stereographic coordinates (ρ, φ) —on the plane in (B1), projected onto the sphere in (B2), resulting in a non-uniform grid in (θ, ϕ) as shown in (B3). (C1) shows a field Ψ defined over (θ, ϕ) , and (C2) shows the same field over (ρ, φ) . In (D), we present field configurations at four time frames: (D1) $t = 0$, (D2) $t = 15$, (D3) $t = 30$, (D4) $t = 45$. Each time frame consists of four three-dimensional plots in embedded (x, y, z) -space: the top row shows the true dynamics, the bottom row shows the neural network predictions; the left column displays the V -field and the right column the W -field of the FitzHugh–Nagumo system.

we do it is provided in Appendix H.2). In (x_1, x_2) -coordinates, the true dynamics are computed by integrating Eq.(6) (Fig. 3A1-4 top row, $V(x_1, x_2, t)$ and $W(x_1, x_2, t)$). In (y_1, y_2) -coordinates, the learned model is integrated from the extrapolated initial condition (see Appendix G for details), and the results are mapped back to (x_1, x_2) (Fig. 3A1-4 bottom row, $\hat{V}(x_1(y_1), x_2(y_2), t)$ and $\hat{W}(x_1(y_1), x_2(y_2), t)$). We observe that the predictions agree, suggesting that our machine learning method not only generalizes across coordinate systems, but also it extends across dimensions. The correct predictions are made in two dimensions, even though the model was trained in one dimension, indicating that the approach is dimension-free.

We now consider the Barkley system, and we show that the learning in 1-D can generalize to **three spatial dimensions** with Neumann (no-flux) boundary conditions on a cubic Cartesian domain $(x_1, x_2, x_3) \in [-L, +L] \times [-L, +L] \times [-L, +L] \equiv \mathcal{C}$, i.e. for all fields Ψ_i .

$$\star d\Psi_i|_{\partial\mathcal{C}} = 0, \quad (13)$$

which is equivalent to stating that the normal derivative $\hat{e}_\perp \cdot \vec{\nabla} \Psi_i$ vanishes on $\partial\mathcal{C}$ (where \hat{e}_\perp is the unit-vector normal to $\partial\mathcal{C}$ locally). These boundary conditions differ from those used during training and in previous cases.

We initialize the Barkley system with a field configuration that clearly displays scroll wave patterns (Appendix H.3). Fig. 3B1–4 shows that the neural network predictions, $\hat{U}(x_1(y_1), x_2(y_2), x_3(y_3), t)$ and $\hat{V}(x_1(y_1), x_2(y_2), x_3(y_3), t)$, closely match the true dynamics, $U(x_1, x_2, x_3, t)$ and $V(x_1, x_2, x_3, t)$, as governed by Eq. (28), demonstrating the adaptability of our dimension-free model to diverse boundary conditions.

4.3 Two-Dimensional Curved Surface Embedded in Three-Dimensional Euclidean Space

Finally, in addition to increasing the number of the spatial dimensions and modifying the boundary conditions, we now *bend the space* (intrinsically). For this case, we explore the dynamics of the FitzHugh–Nagumo fields on a two-dimensional domain (similar to Fig. 3A but not flat) embedded in a spherical surface — a manifold with constant positive intrinsic curvature. We consider two coordinate representations of this curved space — the geographic (θ, ϕ) and the stereographic (ρ, φ) systems — as illustrated in Fig. 4A–C (See Appendix I for more details). The transformation between these coordinate systems is given by:

$$\rho = R \tan(\phi/2), \quad \varphi = \phi, \quad (14)$$

where R is the radius of the sphere. These coordinates can be further related to the Cartesian coordinates (x, y, z) of the ambient three-dimensional Euclidean embedding space via:

$$x = R \sin \theta \sin \phi, \quad y = R \sin \theta \cos \phi, \quad z = R \cos \theta. \quad (15)$$

The spatial domain will be constrained between the radial values ρ_{\min} and ρ_{\max} , and the angular values φ_{\min} and φ_{\max} , which can be determined from θ_{\min} , θ_{\max} , ϕ_{\min} , ϕ_{\max} (Appendix H.4). We impose heterogeneous boundary conditions: the Neumann (no-flux) conditions on the latitude boundaries and the periodic conditions on the longitude boundaries.

We initialize the system with a clearly defined spiral pattern for the fields V and W (defined in (θ, ϕ) -coordinates, see Appendix H.4). The true dynamics — $V(x(\theta, \phi), y(\theta, \phi), z(\theta, \phi), t)$ and $W(x(\theta, \phi), y(\theta, \phi), z(\theta, \phi), t)$ — are obtained by integrating Eq.(6) in (θ, ϕ) -coordinates and then mapped to the embedding space (x, y, z) , as illustrated in the top row of Fig.4D1–4. For the stereographic (ρ, φ) -coordinates, we extrapolate the initial condition (Appendix G), integrate the neural network learned dynamics, and transform the results to (x, y, z) to obtain $\hat{V}(x(\rho, \varphi), y(\rho, \varphi), z(\rho, \varphi), t)$ and $\hat{W}(x(\rho, \varphi), y(\rho, \varphi), z(\rho, \varphi), t)$, shown in the bottom row of Fig.4D1–4. We observe a remarkable agreement (quantified in Appendix J) between both predictions, illustrating that our machine learning method not only generalizes across coordinate systems, extends across dimensions, and adapts to different boundary conditions, but also remains robust under curvatures.

5 Discussion

We have shown that, for certain PDE systems, our approach enables a neural network to learn the evolution operator in a “spatially liberated” manner. The training can be performed using data from simple 1-D numerical simulations or experimental settings, yet it can generalize across dimensions, coordinate systems, and domain curvatures, even when varying boundary conditions. Training can also be performed “fusing” available data from multiple dimensions or geometries. This flexibility makes our approach particularly valuable at the interface between experiments and engineering, as it enables seamless integration of experimental data from different geometry/dimension experiments into predictive models, allowing theoretical frameworks to adapt to complex real-world geometries.

Here, we only focus on second-order PDEs of scalar fields that are invariant under the full local symmetry group of Euclidean space — that is, local orthogonal transformations (rotations and reflections) and local translations (interpreted in the diffeomorphic sense) — which often emerge from long-wavelength physical effective field theories [25, 9]. Next, it would be interesting to consider PDE systems beyond these limitations, such as those involving vector or tensor fields, where additional symmetries and gauge constraints play a role. Further directions include investigating systems with higher-order derivatives, nonlocal interactions, or anisotropic effects to assess the broader applicability of spatially liberated machine learning approach. Notably, we have only considered integer dimensions $n \in \mathbb{N}$, but it would be worthwhile to explore generalizations to fractional dimensions [26, 35, 30, 47]. Additionally, real-world experiments often involve mixed boundary conditions, such as Robin-type boundary conditions [44, 13, 46, 12, 22, 48], which could present another avenue for future investigation. Applications to elliptic, hyperbolic, and more general “mixed” PDE operators can and should also be pursued.

Acknowledgement

The work of I.G.K. and T.V.P. was partially supported by the U.S. Department of Energy and the U.S. National Science Foundation. S.V. was partly supported by NSF CAREER 2339682 and NSF BSF

2430292. We wish to acknowledge valuable discussions with Prof. Dwight Barkley (University of Warwick), who kindly provided us with code for the Barkley model. This preprint has been assigned the number LA-UR-25-24791.

References

- [1] R. Abraham, J. E. Marsden, and T. Ratiu. *Manifolds, tensor analysis, and applications*, volume 75. Springer Science & Business Media, 2012.
- [2] J. Adler. Chemotaxis in bacteria: Motile escherichia coli migrate in bands that are influenced by oxygen and organic nutrients. *Science*, 153(3737):708–716, 1966.
- [3] M. Bär, A. K. Bangia, and I. G. Kevrekidis. Bifurcation and stability analysis of rotating chemical spirals in circular domains: Boundary-induced meandering and stabilization. *Physical Review E*, 67(5):056126, 2003.
- [4] D. Barkley. A model for fast computer simulation of waves in excitable media. *Physica D: Nonlinear Phenomena*, 49(1-2):61–70, 1991.
- [5] J. Blechschmidt and O. G. Ernst. Three ways to solve partial differential equations with neural networks—a review. *GAMM-Mitteilungen*, 44(2):e202100006, 2021.
- [6] S. L. Brunton, J. L. Proctor, and J. N. Kutz. Discovering governing equations from data by sparse identification of nonlinear dynamical systems. *Proceedings of the national academy of sciences*, 113(15):3932–3937, 2016.
- [7] R. L. Bryant, S.-S. Chern, R. B. Gardner, H. L. Goldschmidt, and P. A. Griffiths. *Exterior differential systems*, volume 18. Springer Science & Business Media, 2013.
- [8] R. L. Bryant and N. Durham. Nine lectures on exterior differential systems. *Informal notes for a series of lectures delivered*, pages 12–23, 1999.
- [9] G. Buchalla, O. Catà, and C. Krause. On the power counting in effective field theories. *Physics Letters B*, 731:80–86, 2014.
- [10] M. Cranmer. Interpretable machine learning for science with pysr and symbolicregression. jl. *arXiv preprint arXiv:2305.01582*, 2023.
- [11] S. Cuomo, V. S. Di Cola, F. Giampaolo, G. Rozza, M. Raissi, and F. Piccialli. Scientific machine learning through physics-informed neural networks: Where we are and what’s next. *Journal of Scientific Computing*, 92(3):88, 2022.
- [12] G. D’Aguì, S. A. Marano, and N. S. Papageorgiou. Multiple solutions to a robin problem with indefinite weight and asymmetric reaction. *Journal of Mathematical Analysis and Applications*, 433(2):1821–1845, 2016.
- [13] D. Daners. Principal eigenvalues for generalised indefinite robin problems. *Potential Analysis*, 38:1047–1069, 2013.
- [14] T. Dinesh, M. Haverlaen, and J. Heering. An algebraic programming style for numerical software and its optimization. *Scientific Programming*, 8(4):247–259, 2000.
- [15] M. P. Do Carmo and J. Flaherty Francis. *Riemannian geometry*, volume 2. Springer, 1992.
- [16] G. Fabiani, I. G. Kevrekidis, C. Siettos, and A. N. Yannacopoulos. Randonets: Shallow networks with random projections for learning linear and nonlinear operators. *Journal of Computational Physics*, 520:113433, 2025.
- [17] B. Farb. Representation stability. *arXiv preprint arXiv:1404.4065*, 2014.
- [18] M. L. Frankel and G. I. Sivashinsky. On the nonlinear thermal diffusive theory of curved flames. *Journal de Physique*, 48(1):25–28, Jan. 1987.
- [19] T. Frankel. *The geometry of physics: an introduction*. Cambridge university press, 2011.

- [20] R. González-García, R. Rico-Martínez, and I. G. Kevrekidis. Identification of distributed parameter systems: A neural net based approach. *Computers & chemical engineering*, 22:S965–S968, 1998.
- [21] W. G. Gregory, J. Tonelli-Cueto, N. F. Marshall, A. S. Lee, and S. Villar. Learning equivariant tensor functions with applications to sparse vector recovery. *arXiv preprint arXiv:2406.01552*, 2024.
- [22] K. Gustafson and T. Abe. The third boundary condition—was it robin’s? *The Mathematical Intelligencer*, 20:63–71, 1998.
- [23] J. D. Hunter. Matplotlib: A 2d graphics environment. *Computing in Science & Engineering*, 9(3):90–95, 2007.
- [24] S.-O. Kaba, A. K. Mondal, Y. Zhang, Y. Bengio, and S. Ravanbakhsh. Equivariance with learned canonicalization functions. In *International Conference on Machine Learning*, pages 15546–15566. PMLR, 2023.
- [25] D. B. Kaplan. Five lectures on effective field theory. *arXiv preprint nucl-th/0510023*, 2005.
- [26] G. E. Karniadakis. *Handbook of fractional calculus with applications*, volume 3. De Gruyter Berlin, 2019.
- [27] G. E. Karniadakis, I. G. Kevrekidis, L. Lu, P. Perdikaris, S. Wang, and L. Yang. Physics-informed machine learning. *Nature Reviews Physics*, 3(6):422–440, 2021.
- [28] D. P. Kingma and J. Ba. Adam: A method for stochastic optimization. *arXiv preprint arXiv:1412.6980*, 2014.
- [29] D. Kochkov, J. A. Smith, A. Alieva, Q. Wang, M. P. Brenner, and S. Hoyer. Machine learning–accelerated computational fluid dynamics. *Proceedings of the National Academy of Sciences*, 118(21):e2101784118, 2021.
- [30] A. Kochubei, Y. Luchko, V. E. Tarasov, and I. Petráš. *Handbook of fractional calculus with applications*, volume 1. De Gruyter Berlin, 2019.
- [31] N. Kovachki, Z. Li, B. Liu, K. Azizzadenesheli, K. Bhattacharya, A. Stuart, and A. Anandkumar. Neural operator: Learning maps between function spaces with applications to pdes. *Journal of Machine Learning Research*, 24(89):1–97, 2023.
- [32] K. Krischer, R. Rico-Martínez, I. Kevrekidis, H. Rotermund, G. Ertl, and J. Hudson. Model identification of a spatiotemporally varying catalytic reaction. *AIChE Journal*, 39(1):89–98, 1993.
- [33] S. Lee, Y. M. Psarellis, C. I. Siettos, and I. G. Kevrekidis. Learning black-and gray-box chemotactic pdes/closures from agent based monte carlo simulation data. *Journal of Mathematical Biology*, 87(1):15, 2023.
- [34] E. Levin and M. Díaz. Any-dimensional equivariant neural networks. In *International Conference on Artificial Intelligence and Statistics*, pages 2773–2781. PMLR, 2024.
- [35] A. Lischke, G. Pang, M. Gulian, F. Song, C. Glusa, X. Zheng, Z. Mao, W. Cai, M. M. Meerschaert, M. Ainsworth, et al. What is the fractional laplacian? *arXiv preprint arXiv:1801.09767*, 2018.
- [36] L. Lu, P. Jin, G. Pang, Z. Zhang, and G. E. Karniadakis. Learning nonlinear operators via deep-onet based on the universal approximation theorem of operators. *Nature machine intelligence*, 3(3):218–229, 2021.
- [37] J. E. Marsden and T. J. R. Hughes. *Mathematical Foundations of Elasticity*. Dover Publications, Inc., New York, 1994.
- [38] C. P. Martín-Linares, Y. M. Psarellis, G. Karapetsas, E. D. Koronaki, and I. G. Kevrekidis. Physics-agnostic and physics-infused machine learning for thin films flows: modelling, and predictions from small data. *Journal of Fluid Mechanics*, 975:A41, 2023.

- [39] S. Maskey, R. Levie, and G. Kutyniok. Transferability of graph neural networks: an extended graphon approach. *Applied and Computational Harmonic Analysis*, 63:48–83, 2023.
- [40] J. Masoliver, L. Garrido, and J. Llosa. Geometrical Derivation of the Intrinsic Fokker-Planck Equation and its Stationary Distribution. *Journal of Statistical Physics*, 46(1-2):233–248, Jan. 1987.
- [41] B. McKay. Introduction to exterior differential systems. *arXiv preprint arXiv:1706.09697*, 2017.
- [42] R. J. Morris, T. V. Phan, M. Black, K.-C. Lin, I. G. Kevrekidis, J. A. Bos, and R. H. Austin. Bacterial population solitary waves can defeat rings of funnels. *New Journal of Physics*, 19(3):035002, 2017.
- [43] M. Nakahara. *Geometry, topology and physics*. CRC press, 2018.
- [44] I. Netuka. The robin problem in potential theory (preliminary communication). *Commentationes Mathematicae Universitatis Carolinae*, 12(1):205–211, 1971.
- [45] P. J. Olver. Moving frames. *Journal of Symbolic Computation*, 36(3-4):501–512, 2003.
- [46] N. S. Papageorgiou and V. D. Rădulescu. Multiple solutions with precise sign for nonlinear parametric robin problems. *Journal of Differential Equations*, 256(7):2449–2479, 2014.
- [47] T. V. Phan, T. H. Cai, and V. H. Do. Vanishing in fractal space: Thermal melting and hydrodynamic collapse. *Physics of Fluids*, 36(3), 2024.
- [48] T. V. Phan, S. Li, D. Ferreris, R. Morris, J. Bos, B. Guo, S. Martiniani, P. Chaikin, Y. G. Kevrekidis, and R. H. Austin. Social physics of bacteria: Avoidance of an information black hole. *arXiv preprint arXiv:2401.16691*, 2024.
- [49] T. V. Phan, H. H. Mattingly, L. Vo, J. S. Marvin, L. L. Looger, and T. Emonet. Direct measurement of dynamic attractant gradients reveals breakdown of the patlak–keller–segel chemotaxis model. *Proceedings of the National Academy of Sciences*, 121(3):e2309251121, 2024.
- [50] T. V. Phan, R. Morris, M. E. Black, T. K. Do, K.-C. Lin, K. Nagy, J. C. Sturm, J. Bos, and R. H. Austin. Bacterial route finding and collective escape in mazes and fractals. *Physical Review X*, 10(3):031017, 2020.
- [51] Y. M. Psarellis, S. Lee, T. Bhattacharjee, S. S. Datta, J. M. Bello-Rivas, and I. G. Kevrekidis. Data-driven discovery of chemotactic migration of bacteria via coordinate-invariant machine learning. *BMC bioinformatics*, 25(1):337, 2024.
- [52] M. Raissi, P. Perdikaris, and G. E. Karniadakis. Physics-informed neural networks: A deep learning framework for solving forward and inverse problems involving nonlinear partial differential equations. *Journal of Computational physics*, 378:686–707, 2019.
- [53] L. Ruiz, L. Chamon, and A. Ribeiro. Graphon neural networks and the transferability of graph neural networks. *Advances in Neural Information Processing Systems*, 33:1702–1712, 2020.
- [54] M. Spivak. *A Comprehensive Introduction to Differential Geometry, Volume V*. Publish or Perish, 3rd edition, 1999. See Chapter 13.7: A Smattering of Classical Invariant Theory, Theorem 35.
- [55] M. Velasco, K. O’Hare, B. Rychtenberg, and S. Villar. Graph neural networks and non-commuting operators. *Advances in neural information processing systems*, 37:95662–95691, 2024.
- [56] S. Villar, D. W. Hogg, K. Storey-Fisher, W. Yao, and B. Blum-Smith. Scalars are universal: Equivariant machine learning, structured like classical physics. *Advances in Neural Information Processing Systems*, 34:28848–28863, 2021.
- [57] S. Villar, D. W. Hogg, W. Yao, G. A. Kevrekidis, and B. Schölkopf. Towards fully covariant machine learning. *Transactions on Machine Learning Research*, 2024.

- [58] H. Weyl. *The classical groups: their invariants and representations*, volume 1. Princeton university press, 1946.
- [59] H. Weyl. *Symmetry*. Princeton University Press, 2015.
- [60] S. O. Wilson. Differential Forms, Fluids, and Finite Models. *Proceedings of the American Mathematical Society*, 139(7):2597–2604, Feb. 2011.

A Background on Differential Forms

A differential form is a mathematical object that generalizes scalars, vectors, and volumes, enabling integration and differentiation on manifolds in a coordinate-free and, to some extent, also in a dimension-free manner. A general k -form is a combination of k -differentials:

$$\Omega = \omega_{\mu_1\mu_2\dots\mu_k} dx^{\mu_1} \wedge dx^{\mu_2} \wedge \dots \wedge dx^{\mu_k} , \quad (16)$$

where $\omega_{\mu_1\mu_2\dots\mu_k}$ are asymmetric tensor components, \wedge denotes the wedge product which is anti-commutative, and note that we use the Einstein summation convention unless otherwise specified. On a Riemannian manifold, the contravariant version of these components can be obtained by raising the indices using the inverse metric tensor $g^{\mu\nu}$ (which is the inverse of the symmetric metric tensor $g_{\mu\nu}$, i.e. $g^{\mu\nu}g_{\mu\rho} = \delta^\nu_\rho$, where δ is the Kronecker delta tensor):

$$\omega^{\mu_1\mu_2\dots\mu_k} = g^{\mu_1\nu_1}g^{\mu_2\nu_2}\dots g^{\mu_k\nu_k}\omega_{\nu_1\nu_2\dots\nu_k} . \quad (17)$$

The Hodge star is the operator that turns a k -form into a $(n - k)$ -form:

$$\star\Omega = \frac{k!}{(n - k)!} \epsilon_{\mu_1\mu_2\dots\mu_d} \omega^{\mu_1\mu_2\dots\mu_k} dx^{\mu_{k+1}} \wedge dx^{\mu_{k+2}} \wedge \dots \wedge dx^{\mu_n} , \quad (18)$$

in which $\epsilon_{\mu_1\mu_2\dots\mu_d}$ is the Levi-Civita tensor (exists on orientable manifolds). The exterior derivative $d\Omega$ is a $(k + 1)$ -form, which can be calculated with:

$$d\Omega = d\omega_{\mu_1\mu_2\dots\mu_k} \wedge dx^{\mu_1} \wedge dx^{\mu_2} \wedge \dots \wedge dx^{\mu_{k-1}} \wedge dx^{\mu_k} , \quad (19)$$

where $d\omega_{\mu_1\mu_2\dots\mu_k}$ corresponds to the differential of the component $\omega_{\mu_1\mu_2\dots\mu_k}$, i.e.

$$d\omega_{\mu_1\mu_2\dots\mu_k} = \partial_{\mu_{k+1}}\omega_{\mu_1\mu_2\dots\mu_k} dx^{\mu_{k+1}} . \quad (20)$$

In a coordinate-explicit representation, given the metric structure g defined on the manifold \mathcal{M} , the Laplacians and the inner products can be written as:

- The Laplacians:

$$\star d \star d\Psi_j = |g|^{-1/2} \partial_\mu \left(|g|^{1/2} g^{\mu\nu} \partial_\nu \Psi_j \right) , \quad (21)$$

where $j = 1, 2, 3, \dots$ and $|g|$ is the determinant of the metric tensor $g_{\mu\nu}$. There are N of them in total.

- The inner products:

$$\langle d\Psi_j, d\Psi_k \rangle \equiv \star (d\Psi_j \wedge \star d\Psi_k) = g^{\mu\nu} \partial_\mu \Psi_j \partial_\nu \Psi_k , \quad (22)$$

where $j, k = 1, 2, 3, \dots$. Since these products are symmetric, there are $N(N + 1)/2$ distinct inner products in total.

B Numerical Scheme

To investigate systems of PDEs numerically, we need to specify the differentiation and integration schemes because they govern how the spatio-temporal continuous PDEs are approximated and then solved in a discrete form. The chosen methods influence the accuracy, stability, computational cost, and the appropriateness of the numerical solution.

B.1 Spatial-Differentiation

Here, the continuous spatial-derivatives in the PDEs are replaced by discrete approximations, i.e. central finite differences at the second-order accuracy. For simplicity, we consider the spatial-differentiation, such as ∂_x , ∂_x^2 , of one-dimensional space scalar field, e.g. $M(x, t)$, $N(x, t)$. Generalizing to higher dimensions is straightforward, as each coordinate is treated independently.

For the first spatial-derivative, given that Δx is the spacing between adjacent grid points, we use the following formula at each grid points:

$$\partial_x M(x, t) \stackrel{\text{num}}{\approx} \frac{M(x + \Delta x) - M(x - \Delta x)}{2\Delta x}.$$

For the second spatial-derivative, we apply:

$$\partial_x^2 M(x, t) \stackrel{\text{num}}{\approx} \frac{M(x + \Delta x) - 2M(x) + M(x - \Delta x)}{\Delta x^2}.$$

Note that $\partial_x^2 M(x, t) \stackrel{\text{num}}{\approx} \partial_x [\partial_x M(x, t)]$ up to a small error of order $\mathcal{O}(\Delta x^2)$. When dealing with spatial derivatives inside other spatial derivatives, it can be beneficial to split them out rather than applying the derivatives consecutively before using the numerical approximations, e.g.

$$\partial_x [N(x, t) \partial_x M(x, t)] \rightarrow \partial_x N(x, t) \partial_x M(x, t) + N(x, t) \partial_x^2 M(x, t) \stackrel{\text{num}}{\approx} \dots \quad (23)$$

This splitting helps control error propagation, maintains higher accuracy, and also provides better handling of boundary conditions, preventing error accumulation near boundaries.

When considering a finite domain e.g. $x \in [-L_x, +L_x]$, the boundary conditions at the edges of the domain i.e. $x = \mp L_x$ dictate how we should modify Eq. (B.1) and Eq. (B.1) for points lying outside of the domain. For examples:

- Periodic boundary conditions:

$$M(\mp L_x \mp \Delta x) = M(\pm L_x). \quad (24)$$

- Neumann (no-flux) boundary conditions:

$$M(\mp L_x \mp \Delta x) = M(\mp L_x). \quad (25)$$

We can see directly from this identification that $\partial_x M(x = \mp L_x) = 0$.

B.2 Temporal-Integration

Here, we use the forward Euler method to discretize the time derivative with spacing Δt :

$$\partial_t M(x, t) \stackrel{\text{num}}{\approx} \frac{M(x, t + \Delta t) - M(x, t)}{\Delta t}, \quad (26)$$

thus:

$$\partial_t M(x, t) = \mathcal{F}(t) \implies M(x, t + \Delta t) = M(x, t) + \mathcal{F}(t) \Delta t, \quad (27)$$

where \mathcal{F} is a function that can depend not only on time position t , but also on space location, the fields value, and their spatial-derivatives e.g. the right-hand-side of the PDE. To numerically integrate $M(x, t)$, given the initial field value, we use Eq. (27) consecutively every timestep $t \rightarrow t + \Delta t$.

C Equations in Coordinate-Explicit Forms

Barkley System: In coordinate-explicit form, the Barkley system (Equation 8) is expressed as

$$\begin{aligned} \partial_t U(x, t) &= \bar{\nabla}^2 U(x, t) + \frac{1}{\varepsilon} U(x, t) [1 - U(x, t)] \left[U(x, t) - \frac{V(x, t) + b}{a} \right], \\ \partial_t V(x, t) &= U(x, t) - V(x, t), \end{aligned} \quad (28)$$

Modified Patlak-Keller-Segel System: In coordinate-explicit form, the Modified Patlak-Keller-Segel System 9) is expressed as

$$\begin{aligned}\partial_t A(x, t) &= \vec{\nabla}^2 A(x, t) - \left[\frac{A(x, t)}{1 + A(x, t)} \right] \left[\frac{B(x, t)}{1 + B(x, t)} \right], \\ \partial_t B(x, t) &= \alpha B(x, t) + \vec{\nabla}^2 [D_B B(x, t)] \\ &\quad - \vec{\nabla} \left(\chi_0 \left[\frac{B(x, t)}{1 + B(x, t)/B_h} \right] \vec{\nabla} \left\{ \ln \left[1 + \frac{A(x, t)}{K_i} \right] \right\} \right),\end{aligned}\tag{29}$$

D Training the Neural Networks

We describe the training procedure and also the generation of training data within a one-dimensional periodic space equipped with a Cartesian coordinate where we impose periodic boundary conditions (Appendix B), i.e.

$$x \in \mathcal{S} = [-L, +L], \quad x \sim x + L, \tag{30}$$

and its use in training spatially liberated neural networks for each system as sketched in Fig. 1A.

For each of the systems (FitzHugh-Nagumo model, Barkley model, and Patlak-Keller-Segel model), we aim to train a neural network with an MLP architecture, consisting of $n_{\text{layer}} = 2$ hidden layers, each with n_{neuron} neurons (to be specified). This network takes as input seven scalar quantities (0-forms) which are invariant features as listed in Eq. (5):

$$\Psi_1, \langle d\Psi_1, d\Psi_1 \rangle, \star d \star d\Psi_1, \Psi_2, \langle d\Psi_2, d\Psi_2 \rangle, \star d \star d\Psi_2, \langle d\Psi_1, d\Psi_2 \rangle \tag{31}$$

to predict two changing rates of the dynamical fields

$$\partial_t \Psi_1, \partial_t \Psi_2$$

at each location x in space and point t in time; see Fig. 1A. For the FitzHugh-Nagumo system (Section 3.1), we set $n_{\text{neuron}} = 64$, with the fields identified as $(\Psi_1, \Psi_2) = (V, W)$. In the Barkley system (Section 3.2), we likewise use $n_{\text{neuron}} = 64$, where $(\Psi_1, \Psi_2) = (U, V)$. With the Patlak-Keller-Segel system (Section 3.3), we consider $n_{\text{neuron}} = 32$, in which $(\Psi_1, \Psi_2) = (A, B)$.

The training data for each case is first simulated and then subsampled for training as described below: Section D.1 for the FitzHugh-Nagumo system, Section D.2 for the Barkley system, and Section D.3 for the modified Patlak-Keller-Segel system. For all simulations in this work, we have checked that the numerical computations are robust to space-time discretizations.

All computations in this work were performed on CPU-based machines. Each experiment was trained in under one hour using an internal compute node equipped with an Intel Core i7-7700 processor (3.60 GHz), 128 GB RAM, and local SSD storage. No GPUs or cloud services were used.

D.1 FitzHugh-Nagumo System Training

We generate numerical simulation data of the FitzHugh-Nagumo system on a one-dimensional domain specified in Eq. (30), using $L = 10^2$. The spatiotemporal discretization is set to $(\Delta t, \Delta x) = (10^{-1}, 1)$, and for every numerical simulation of Eq. (7) we generate the time progression consecutively at each timestep Δt , using forward Euler method Eq. (27), for $t \in [0, T]$ where $T = 10^3$. All training data is obtained from a single simulation, in which the initial field configuration — consisting of combinations of a few localized configurations — is given in Appendix E.1. Then, we randomly-selected a subset of the simulation data (i.e. 10%) to create the training dataset for neural network training. This reduces the training data size but still ensures a fine time-increment, minimizing error propagation and improving long-term prediction accuracy of the trained model. The neural network model is optimized using the least squares deviation criterion with the Adam optimizer [28], set to a learning rate of 5×10^{-4} , and trained for 2×10^3 epochs.

D.2 Barkley System Training

We create numerical simulation data on the one-dimensional domain specified in Eq. (30) for Barkley system, using $L = 5 \times 10^1$. The spatiotemporal discretization is set to $(\Delta t, \Delta x) = (10^{-2}, 5 \times 10^{-1})$,

and for every numerical simulation of Eq. (8) we generate the time progression consecutively at each timestep Δt , using the forward Euler method Eq. (27), for $t \in [0, T]$ where $T = 2 \times 10^2$. All training data is obtained from a single simulation, in which the initial field configuration — consisting of combinations of a few localized configurations — is given in Appendix E.2. Then, we randomly-selected a subset of the simulation data (i.e. 5%) to create the training dataset for neural network training. This reduces the training data size but still ensures a fine time-increment, minimizing error propagation and improving long-term prediction accuracy of the trained model. The neural network model is optimized using the least squares deviation criterion with the Adam optimizer, set to a learning rate of 5×10^{-4} , and trained for 2×10^3 epochs.

D.3 Patlak-Keller-Segel System Training

We produce numerical simulation data for the Palak-Keller-Segel system on a one-dimensional domain specified in Eq. (30), using $L = 10^2$. The spatiotemporal discretization is set to $(\Delta t, \Delta x) = (10^{-1}, 1)$, and for every numerical simulation of Eq. (9) we generate the time progression consecutively at each timestep Δt , using forward Euler method Eq. (27), for $t \in [0, T]$ where $T = 5 \times 10^2$. The training data is derived from multiple simulations showcasing traveling wave collisions and diffusion. The initial field configurations used to create these simulations are uniform for A and consist of combinations of a few localized configurations for B , as provided in Appendix E.3. Our choice of domain dimensions and initial field configurations are motivated by their relevance to real experimental settings using microfluidic devices. Then, we randomly-selected a subset of the simulation data (i.e. 2%) to create the training dataset for neural network training. This reduces the training data size but still ensures a fine time-increment, minimizing error propagation and improving long-term prediction accuracy of the trained model. The neural network model is optimized using the least squares deviation criterion with the Adam optimizer, set to a learning rate of 5×10^{-4} , and trained for 2×10^3 epochs.

For notational convenience, we redefine A, B to represent the normalized quantities $A/A_{\max}, B/B_{\max}$ respectively. This convention applies from this point forward unless specified otherwise. Note that $A_{\max} = 30$ and $B_{\max} = 1$.

E Initial Field Configurations for Training

Here we list the initial field configurations used to generate the training data for the FitzHugh-Nagumo, the Barkley, and the Patlak-Keller-Segel models, as explained in Appendix D.

E.1 FitzHugh-Nagumo system

The initial field configurations are given by:

$$\begin{aligned} V(x, 0) &= V_{01} \exp \left[-\frac{(x - x_{V1})^2}{2\sigma_{xV1}} \right] + V_{02} \exp \left[-\frac{(x - x_{V2})^2}{2\sigma_{xV2}} \right], \\ W(x, 0) &= W_{01} \exp \left[-\frac{(x - x_{W1})^2}{2\sigma_{xW1}} \right], \end{aligned} \quad (32)$$

where:

$$\begin{aligned} (V_{01}, x_{V1}, \sigma_{xV1}) &= (+2, +40, 10), \\ (V_{02}, x_{V2}, \sigma_{xV2}) &= (-2, -40, 10), \\ (W_{01}, x_{W1}, \sigma_{xW1}) &= (+1, 0, 10). \end{aligned} \quad (33)$$

E.2 Barkley system

The initial field configurations are given by:

$$\begin{aligned}
U(x, 0) &= U_{01} \exp \left[-\frac{(x - x_{U1})^2}{2\sigma_{xU1}} \right] \\
&+ U_{02} \exp \left[-\frac{(x - x_{U2})^2}{2\sigma_{xU2}} \right] + U_{03} \exp \left[-\frac{(x - x_{U3})^2}{2\sigma_{xU3}} \right], \\
V(x, 0) &= V_{01} \exp \left[-\frac{(x - x_{V1})^2}{2\sigma_{xV1}} \right] \\
&+ V_{02} \exp \left[-\frac{(x - x_{V2})^2}{2\sigma_{xV2}} \right] + V_{03} \exp \left[-\frac{(x - x_{V3})^2}{2\sigma_{xV3}} \right],
\end{aligned} \tag{34}$$

where:

$$\begin{aligned}
(U_{01}, x_{U1}, \sigma_{xU1}) &= (0.9, +22, 4), \\
(U_{02}, x_{U2}, \sigma_{xU2}) &= (0.5, -8, 4), \\
(U_{03}, x_{U3}, \sigma_{xU3}) &= (0.8, -28, 2), \\
(V_{01}, x_{V1}, \sigma_{xV1}) &= (0.5, 0, 4), \\
(V_{02}, x_{V2}, \sigma_{xV2}) &= (0.9, 20, 2), \\
(V_{03}, x_{V3}, \sigma_{xV3}) &= (0.7, -24, 2).
\end{aligned} \tag{35}$$

E.3 Patlak-Keller-Segel system

Here we consider an active matter system of many chemotactic bacteria that navigate in response to chemo-attractants, which they simultaneously deplete through their own consumption [49]. Two important phenomena emerge from bacterial collective chemotaxis: the formation of traveling bands of bacteria and the collisions of those bands, which then diffuse [50]. To generate a series of *in silico* experiments illustrating both phenomena, we begin with simple initial conditions: the Asp is uniform, and bacteria are inoculated at two ports, each modeled by a Gaussian distribution. We consider four different initial profiles for Asp concentration and four times three distinct initial profiles for the bacterial field, i.e.

$$\begin{aligned}
A(x, 0) &= A_0, \\
B(x, 0) &= B_1 \exp \left[-\frac{(x - x_{B1})^2}{2\sigma_{B1}} \right] + B_2 \exp \left[-\frac{(x - x_{B2})^2}{2\sigma_{B2}} \right],
\end{aligned} \tag{36}$$

where:

$$\begin{aligned}
x_{B1} &= -50, \quad x_{B2} = +50, \quad \sigma_{B1} = \sigma_{B2} = 5, \\
A_0 &\in A_{\max} \times \{0, 1/4, 1/2, 3/4, 1\}, \\
B_1 &\in B_{\max} \times \{1/3, 2/3, 1\}, \quad B_2 \in B_{\max} \times \{0, 1/3, 2/3, 1\}.
\end{aligned} \tag{37}$$

For notational convenience, we redefine A, B to represent the normalized quantities $A/A_{\max}, B/B_{\max}$ respectively. This convention applies from this point forward unless specified otherwise. Note that $A_{\max} = 30$ and $B_{\max} = 1$. We have chosen the parameters so that these experiments are implementable within microfluidic environment.

F Cartesian and Non-Cartesian Coordinates

Here we show the relation between different choices of coordinate systems used in Section 4.1 and Section 4.2, from the mapping between locations to the calculation of relevant differential forms.

F.1 Inverse Function and Illustration of y vs x

The inverse function, which helps calculating y from x , is given by:

$$y = f^{-1}(x) = \lambda \left[\frac{\Theta(x)}{\sqrt[3]{2} \cdot 3^{2/3}} - \frac{\sqrt[3]{\frac{2}{3}}}{\Theta(x)} \right], \tag{38}$$

where

$$\Theta(x) = \sqrt[3]{\sqrt{3}\sqrt{27\left(\frac{2x}{\lambda}\right)^2 + 4} + 9\left(\frac{2x}{\lambda}\right)}.$$

The transformations between Cartesian and non-Cartesian coordinates in different spaces are presented in Fig. 5.

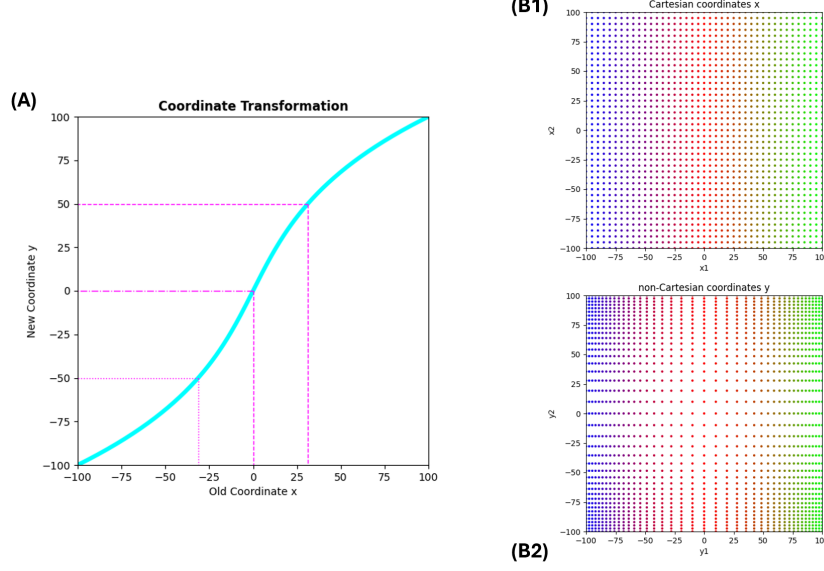


Figure 5: The Cartesian and non-Cartesian coordinate systems in one- and two-dimensional space. Here we use Eq. (11) and Eq. (12) with $\lambda = L = 10^2$. **(A)** One-dimensional space, conversion between x and y . **(B)** Two-dimensional space, conversion between (x_1, x_2) and (y_1, y_2) . The color transitions linearly with x_1 , following the Python Matplotlib `brg` colormap [23], shifting from blue to red to green.

F.2 Calculation of Differential-Forms in One-Dimensional Euclidean Space

Denote $' = d/dy$ when taking the derivative of the function $f(y)$. The differential-form inputs (besides Ψ_1 and Ψ_2) used in the neural network as illustrated in Fig. 1B for the one-dimensional non-Cartesian case (Section 4.1) can be calculated as follows:

- The Laplacians:

$$\star d \star d\Psi_j(t) = \frac{1}{|f'(y)|} \left\{ \frac{|f'(y)|}{[f'(y)]^2} \right\}' \partial_y \Psi_j(y, t) + \frac{1}{[f'(y)]^2} \partial_y^2 \Psi_j(y, t), \quad (39)$$

where $j = 1, 2$. There are two of such inputs.

- The inner products:

$$\langle d\Psi_j(t), d\Psi_k(t) \rangle = \left[\frac{1}{f'(y)} \partial_y \Psi_j(y, t) \right] \left[\frac{1}{f'(y)} \partial_y \Psi_k(y, t) \right], \quad (40)$$

where $j, k = 1, 2$. There are three of such inputs, corresponding to three distinct inner products.

F.3 Calculation of Differential-Forms in Two-Dimensional Euclidean Space

The differential-form inputs (besides Ψ_1 and Ψ_2) used in the neural network as illustrated in Fig. 1B for the two-dimensional non-Cartesian case (Section 4.2) can be calculated as follows:

- The Laplacians:

$$\begin{aligned}
\star d \star d \Psi_j(t) &= \frac{1}{|f'(y_1)f'(y_2)|^{1/2}} \partial_{y_1} \left\{ \frac{|f'(y_1)f'(y_2)|^{1/2}}{[f'(y_1)]^2} \right\} \partial_{y_1} \Psi_j(y_1, y_2, t) \\
&+ \frac{1}{|f'(y_1)f'(y_2)|^{1/2}} \partial_{y_2} \left\{ \frac{|f'(y_1)f'(y_2)|^{1/2}}{[f'(y_2)]^2} \right\} \partial_{y_2} \Psi_j(y_1, y_2, t) \\
&+ \frac{1}{[f'(y_1)]^2} \partial_{y_1}^2 \Psi_j(y_1, y_2, t) + \frac{1}{[f'(y_2)]^2} \partial_{y_2}^2 \Psi_j(y_1, y_2, t),
\end{aligned} \tag{41}$$

where $j = 1, 2$. There are two of such inputs.

- The inner products:

$$\begin{aligned}
\langle d \Psi_j(t), d \Psi_k(t) \rangle &= \left[\frac{1}{f'(y_1)} \partial_{y_1} \Psi_j(y_1, y_2, t) \right] \left[\frac{1}{f'(y_1)} \partial_{y_1} \Psi_k(y_1, y_2, t) \right] \\
&+ \left[\frac{1}{f'(y_2)} \partial_{y_2} \Psi_j(y_1, y_2, t) \right] \left[\frac{1}{f'(y_2)} \partial_{y_2} \Psi_k(y_1, y_2, t) \right],
\end{aligned} \tag{42}$$

where $j, k = 1, 2$. There are three of such inputs, corresponding to three distinct inner products.

G Comparison between Different Coordinate Systems

We illustrate the comparison between coordinate systems — using 1D Cartesian and non-Cartesian coordinates as an example — which naturally extends to higher dimensions and curved spaces. For a given dynamical system, we initialize a condition (distinct from the training set) in x -space with uniform Δx discretization. We then compute its evolution via both the true PDE and the neural network model from Section D, showing strong agreement. The corresponding initial condition in y -space (with uniform Δy) is evolved using the neural network, then mapped back to x -space via Eq. (11) for direct comparison. These steps are summarized in Fig. 6. For a coordinate-free model, all these generated datasets should be consistent, which we confirm through our results.

H Initial Field Configurations for Testing

Here we list the initial field configurations used for testing in Section 4.1 (see Appendix H.1), Section 4.2 (see Appendix H.2), Section 4.2 (see Appendix H.3), and Section 4.3 (see Appendix H.4).

H.1 One-Dimensional Euclidean Space

In this case (Section 4.1), we work with the Patlak-Keller-Segel system. The initial field configurations The initial field configurations used in testing follow similar structure to Eq. (37), with:

$$\begin{aligned}
x_{B1} = 10, \quad x_{B2} = -60, \quad \sigma_{B1} = 5, \quad \sigma_{B2} = 6, \\
A_0 = 5/6, \quad B_1 = 0.7, \quad B_2 = 0.4.
\end{aligned} \tag{43}$$

We consider the same periodic space as in Appendix D for Patlak-Keller-Segel system, i.e. $x \in [-L, +L]$ with $L = 10^2$ and a uniform grid of $\Delta x = 1$. The transformation from this Cartesian coordinate x to a non-Cartesian one y follows Eq. (11). We use $y \in [-L, +L]$ with a uniform grid and a lattice spacing of $\Delta y = 1$ when predicting the field evolution dynamics by integrating the trained neural network model from Section E.3 in this coordinate system.

We start with an initial field configuration that has not been used to generate the training data in Appendix D. The field A is uniform everywhere and the field B are combinations of localized configurations, as provided in Eq. (43). We create the field evolution dynamics using the timestep $\Delta t = 10^{-1}$ for $t \in [0, 5 \times 10^2]$ by numerically integrating the PDEs Eq. (29).

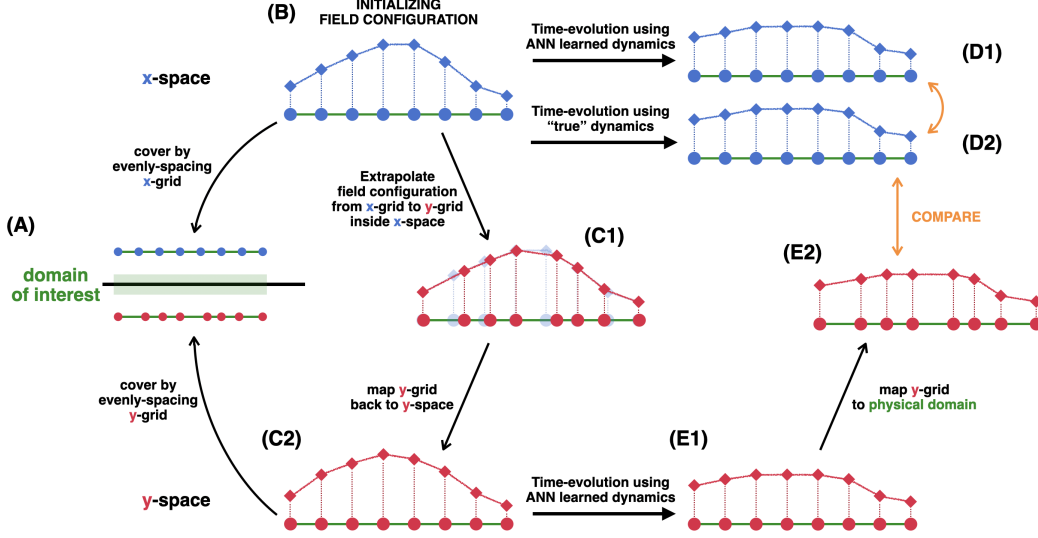


Figure 6: Testing coordinate-free learning in one-dimensional space. We study the time-evolution in different coordinates, using both “true” computed dynamics and ANN learned dynamics. (A) The physical domain of interest can be described (parametrized) by either the x -coordinate or the y -coordinate. An evenly-spaced x -grid is not equivalent to an evenly-spaced y -grid. (B) We start with an initial field configuration in x -space. (C1,C2) We extrapolate the values of the initial field configuration from what it looks like in x -space to its estimation in y -space. (D) In x -space, we compute the time-evolution of the field in two different ways: using the “true dynamics” (D1) and using the neural network learned dynamics (D2). We then can compare them. (E1) In y -space, we compute the time-evolution of the field using the neural network learned dynamics. (E2) We map the field back to physical space, showing what it looks like in x -space, then compare with (D).

H.2 Two-Dimensional Euclidean Space

In this case (Section 4.2), we work with the FitzHugh-Nagumo system. We start with the field configuration given by:

$$\begin{aligned}
 V(x_1, x_2) &= V_{01} \exp \left[-\frac{(x_1 - x_{1V1})^2}{2\sigma_{x1V1}} - \frac{(x_2 - x_{2V1})^2}{2\sigma_{x2V1}} \right] \\
 &\quad + V_{02} \exp \left[-\frac{(x_1 - x_{1V2})^2}{2\sigma_{x1V2}} - \frac{(x_2 - x_{2V2})^2}{2\sigma_{x2V2}} \right], \\
 W(x_1, x_2) &= W_{01} \exp \left[-\frac{(x_1 - x_{1W1})^2}{2\sigma_{x1W1}} - \frac{(x_2 - x_{2W1})^2}{2\sigma_{x2W1}} \right],
 \end{aligned} \tag{44}$$

where:

$$\begin{aligned}
 (V_{01}, x_{1V1}, x_{2V1}, \sigma_{x1V1}, \sigma_{x2V1}) &= (+1, 0, 0, 15, 10), \\
 (V_{02}, x_{1V2}, x_{2V2}, \sigma_{x1V2}, \sigma_{x2V2}) &= (+1, 0, +40, 8, 8), \\
 (W_{01}, x_{1W1}, x_{2W1}, \sigma_{x1W1}, \sigma_{x2W1}) &= (+1, +10, 0, 10, 25).
 \end{aligned} \tag{45}$$

Both V and W are combinations of localized configurations. Then, we numerically integrate the PDEs Eq. (6) for the total amount of time $\Delta T = 8 \times 10^2$ (so that the system has reached the stage of steady spiral wave generation) from the above configurations. We use the final-time configuration as the initial field configuration for the study in Section 4.2.

Consider the periodic spatial domain $(x_1, x_2) \in [-L, +L] \times [-L, +L]$ with $L = 10^2$ and uniform grid of lattice-spacing $(\Delta x_1, \Delta x_2) = (1, 1)$. The transformation from these Cartesian coordinates (x_1, x_2) to non-Cartesian ones (y_1, y_2) is as described Eq. (12). We use $(y_1, y_2) \in [-L, +L] \times [-L, +L]$ with a uniform grid and a lattice-spacing of $(\Delta y_1, \Delta y_2) = 1$ to describe the same space in this new coordinate system.

Since (x_1, x_2) -grid and (y_1, y_2) -grid do not represent identical set of physical points, we need to extrapolate the configuration Eq. (45) to (y_1, y_2) -coordinate. We generate the field evolution dynamics using the timestep $\Delta t = 10^{-1}$ for $t \in [0, 10^2]$, in different coordinate systems.

H.3 Three-Dimensional Euclidean Space

In this case (Section 4.2), we work with the Barkley system. We start with the field configuration given by:

$$\begin{aligned}
U(x_1, x_2, x_3) &= U_{01} \exp \left[-\frac{(x_1 - x_{1U1})^2}{2\sigma_{x1U1}} - \frac{(x_2 - x_{2U1})^2}{2\sigma_{x2U1}} - \frac{(x_3 - x_{3U1})^2}{2\sigma_{x3U1}} \right] \\
&+ U_{02} \exp \left[-\frac{(x_1 - x_{1U2})^2}{2\sigma_{x1U2}} - \frac{(x_2 - x_{2U2})^2}{2\sigma_{x2U2}} - \frac{(x_3 - x_{3U2})^2}{2\sigma_{x3U2}} \right], \\
V(x_1, x_2, x_3) &= V_{01} \exp \left[-\frac{(x_1 - x_{1V1})^2}{2\sigma_{x1V1}} - \frac{(x_2 - x_{2V1})^2}{2\sigma_{x2V1}} - \frac{(x_3 - x_{3V1})^2}{2\sigma_{x3V1}} \right] \\
&+ V_{02} \exp \left[-\frac{(x_1 - x_{1V2})^2}{2\sigma_{x1V2}} - \frac{(x_2 - x_{2V2})^2}{2\sigma_{x2V2}} - \frac{(x_3 - x_{3V2})^2}{2\sigma_{x3V2}} \right],
\end{aligned} \tag{46}$$

where:

$$\begin{aligned}
(U_{01}, x_{1U1}, x_{2U1}, x_{3U1}, \sigma_{x1U1}, \sigma_{x2U1}, \sigma_{x3U1}) &= (0.5, 0, 6, 0, 5, 6, 5), \\
(U_{02}, x_{1U2}, x_{2U2}, x_{3U2}, \sigma_{x1U2}, \sigma_{x2U2}, \sigma_{x3U2}) &= (0.5, 0, 12, 6, 4, 5, 4), \\
(V_{01}, x_{1V1}, x_{2V1}, x_{3V1}, \sigma_{x1V1}, \sigma_{x2V1}, \sigma_{x3V1}) &= (0.8, 5, 6, 0, 5, 4, 4), \\
(V_{02}, x_{1V2}, x_{2V2}, x_{3V2}, \sigma_{x1V2}, \sigma_{x2V2}, \sigma_{x3V2}) &= (0.7, -7, 6, -7, 4, 4, 6).
\end{aligned} \tag{47}$$

Both U and V are combinations of localized configurations. Then, we numerically integrate the PDEs Eq. (28) for the total amount of time $\Delta T = 2 \times 10^1$ (so that the system has reached the stage of steady scroll wave generation) from the above configurations. We use the final-time configuration as the initial field configuration for the study in Section 4.2.

We consider the confined space $(x_1, x_2, x_3) \in [-L, +L] \times [-L, +L] \times [-L, +L]$ with $L = 5 \times 10^1$, covered by a uniform grid of lattice-spacing $(\Delta x_1, \Delta x_2, \Delta x_3) = (5 \times 10^{-1}, 5 \times 10^{-1}, 5 \times 10^{-1})$. We compute the field evolution dynamics in this Cartesian coordinate system using the timestep $\Delta t = 10^{-2}$ for $t \in [0, 5]$.

H.4 A Two-Dimensional, Intrinsically Curved Surface

In this case (Section 4.3), we work with the FitzHugh-Nagumo system. On the spherical surface, the FitzHugh-Nagumo system (Section 3.1) written in the (θ, ϕ) -coordinate can be described by the following PDEs:

$$\begin{aligned}
\partial_t V(\theta, \phi, t) &= \frac{1}{R^2} \left(\cot \theta \partial_\theta + \partial_\theta^2 + \frac{1}{\sin^2 \theta} \partial_\phi^2 \right) V(\theta, \phi, t) \\
&+ V(\theta, \phi, t) - \frac{1}{3} V^3(\theta, \phi, t) - W(x, t), \\
\partial_t W(\theta, \phi, t) &= \varepsilon [V(\theta, \phi, t) + \beta - \gamma W(\theta, \phi, t)].
\end{aligned} \tag{48}$$

We start with the field configuration given by:

$$\begin{aligned}
V(\rho, \varphi, 0) &= V_{01} \exp \left[-\frac{(\rho - \rho_{V1})^2}{2\sigma_{\rho V1}} - \frac{(\varphi - \varphi_{V1})^2}{2\sigma_{\varphi V1}} \right] \\
&+ V_{02} \exp \left[-\frac{(\rho - \rho_{V2})^2}{2\sigma_{\rho V2}} - \frac{(\varphi - \varphi_{V2})^2}{2\sigma_{\varphi V2}} \right], \\
W(\rho, \varphi, 0) &= W_0 \exp \left[-\frac{(\rho - \rho_W)^2}{2\sigma_{\rho W}} - \frac{(\varphi - \varphi_W)^2}{2\sigma_{\varphi W}} \right].
\end{aligned} \tag{49}$$

where:

$$\begin{aligned}
(V_{01}, \rho_{V1}, \varphi_{V1}, \sigma_{\rho V1}, \sigma_{\varphi V1}) &= (1, 140, \pi/6, 15, 0.15), \\
(V_{02}, \rho_{V2}, \varphi_{V2}, \sigma_{\rho V2}, \sigma_{\varphi V2}) &= (1, 160, \pi/4, 10, 0.1), \\
(W_0, \rho_W, \varphi_W, \sigma_{\rho W}, \sigma_{\varphi W}) &= (1, 150, \pi/4, 10, 0.2).
\end{aligned} \tag{50}$$

Both V and W are combinations of localized configurations. Then, we numerically integrate the PDEs Eq. (48) for the total amount of time $\Delta T = 2 \times 10^2$ (so that the system has reached the stage of steady spiral wave generation) from the above configurations. We use the final-time configuration as the initial field configuration for the study in Section 4.3.

We work on the spherical surface of radius $R = 2 \times 10^2$, analyzing the two-dimensional curved space covered by $(\rho, \varphi) \in [\rho_{\min}, \rho_{\max}] \times [\varphi_{\min}, \varphi_{\max}]$, where $\rho_{\min} = 5 \times 10^1$, $\rho_{\max} = 2 \times 10^2$ and $\varphi_{\min} = 0$, $\varphi_{\max} = \pi/2$. We discretize the coordinates (ρ, φ) uniformly with the lattice-spacing

$$(\Delta\rho, \Delta\varphi) = \left(\frac{\rho_{\max} - \rho_{\min}}{300}, \frac{\varphi_{\max} - \varphi_{\min}}{200} \right). \quad (51)$$

The transformation from these stereographic coordinates (ρ, φ) to geographical ones (θ, ϕ) is as described Eq. (14). We use $(\theta, \phi) \in [-L, +L] \times [\theta_{\min}, \theta_{\max}] \times [\phi_{\min}, \phi_{\max}]$ to describe the same space in this new coordinate system, where we use a uniform grid with the lattice-spacing

$$(\Delta\theta, \Delta\phi) = \left(\frac{\theta_{\max} - \theta_{\min}}{300}, \frac{\phi_{\max} - \phi_{\min}}{200} \right). \quad (52)$$

Note that the (ρ, φ) -grid and the (θ, ϕ) -grids are not comprised of identical sets of physical points. We compute the field evolution dynamics on the spherical surface in this different coordinate system, using the timestep $\Delta t = 10^{-1}$ for $t \in [0, 5 \times 10^1]$.

I Geographic and Stereographic Coordinates

We consider a sphere of radius R , equipped with geographical-coordinates (θ, ϕ) corresponding to spherical-angles, where $\theta = 0$ represents the South pole and $\theta = \pi$ is the North pole. The spherical surface can be embedded in a three-dimensional Euclidean space via Eq. (15), where (x, y, z) are the corresponding Cartesian coordinates. On this curved manifold, the induced metric is given by:

$$ds^2 = R^2 (d\theta^2 + \sin^2 \theta d\phi^2). \quad (53)$$

There, Laplacians and the inner-products can be calculated from:

- The Laplacians:

$$\star d \star d\Psi_j = \frac{1}{R^2} \left(\cot \theta \partial_\theta \Psi_j + \partial_\theta^2 \Psi_j + \frac{1}{\sin^2 \theta} \partial_\phi^2 \Psi_j \right), \quad (54)$$

where $j = 1, 2$. There are two of them.

- The inner products:

$$\langle d\Psi_j, d\Psi_k \rangle = \frac{1}{R^2} \left(\partial_\theta \Psi_j \partial_\theta \Psi_k + \frac{1}{\sin^2 \theta} \partial_\phi \Psi_j \partial_\phi \Psi_k \right), \quad (55)$$

where $j, k = 1, 2$. There are three distinct inner products.

We study a region of the sphere surface bounded by latitude θ_{\min} and θ_{\max} , and by longitude ϕ_{\min} and ϕ_{\max} . We also impose the Neumann (no-flux) conditions as described in Eq. (13) on the latitude boundaries and the periodic conditions on the longitude boundaries.

We focus on a projection that utilizes the South pole as the projection viewpoint and the equator plane as the projection plane. A convenient mapping — written in stereographic polar-coordinates — is as introduced in Eq. (14). Thus, the metric in Eq. (53) after this coordinate transformation becomes:

$$ds^2 = \left[\frac{4R^4}{(R^2 + \rho^2)^2} \right] (d\rho^2 + \rho^2 d\varphi^2). \quad (56)$$

The Laplacians and the inner-products in these new coordinates can be expressed with:

- The Laplacians:

$$\star d \star d\Psi_j = \left[\frac{(R^2 + \rho^2)^2}{4R^4} \right] \left(\frac{1}{\rho} \partial_\rho \Psi_j + \partial_\rho^2 \Psi_j + \frac{1}{\rho^2} \partial_\varphi^2 \Psi_j \right), \quad (57)$$

where $j = 1, 2$. There are two of them.

- The inner products:

$$\langle d\Psi_j, d\Psi_k \rangle = \left[\frac{(R^2 + \rho^2)^2}{4R^4} \right] \left(\partial_\rho \Psi_j \partial_\rho \Psi_k + \frac{1}{\rho^2} \partial_\phi \Psi_j \partial_\phi \Psi_k \right), \quad (58)$$

where $j, k = 1, 2$. There are three distinct inner products.

In this coordinate system, the spatial domain of interests is bound between radius ρ_{\min} and ρ_{\max} , and angle φ_{\min} and φ_{\max} , which can be determined from $\theta_{\min}, \theta_{\max}, \phi_{\min}, \phi_{\max}$, with Eq. (14). Figure 4A-C illustrates how geographical coordinates (θ, ϕ) and stereographic coordinates (ρ, φ) are related through a projection from the South pole onto the equatorial plane. It shows that the same region on the surface of the sphere can be covered by evenly-spacing grids in both coordinate systems, even though these grids are not equivalent.

We aim to demonstrate that, using the neural network model trained in one dimension in Sec. D, we can predict the correct field evolution dynamics on the surface of the sphere regardless of the chosen coordinate system. In other words, not only do we need to generate a prediction, but also compare it with the expected true dynamics. We begin with an initial condition defined in (θ, ϕ) -space with uniform $(\Delta\theta, \Delta\phi)$ discretization. We then compute the field evolution in the (θ, ϕ) -coordinate using direct integration of the true PDE. Next, we determine by extrapolation the corresponding initial condition in (ρ, φ) -space with uniform $(\Delta\rho, \Delta\varphi)$ discretization and use it to generate the field evolution in (ρ, φ) -coordinates via the trained neural network model in Section D. To make comparison, we transform both the generated datasets to the three-dimensional Euclidean (x, y, z) -space. These steps are similar to what has been demonstrated for one-dimensional case, see Fig. 6. For our spatially liberated neural network model, all these generated datasets are expected to be in agreement, which we confirm through our results.

J Comparing “True” and Learned Dynamics

To compare the “true” dynamics $\Psi_i(\zeta, t)$ with the neural learned dynamics $\hat{\Psi}(\eta, t)$ (which computed at different locations), we extrapolate from $\hat{\Psi}$ evaluated at η -locations to its corresponding values at ζ -locations, denoted as $\tilde{\Psi}_i(\eta, t)$. We then can calculate $\Psi_i - \tilde{\Psi}_i$ to see the deviation between these dynamics and report the mean square-error (MSE) for all cases.

J.1 1-, 2- and 3-Dimensional Euclidean Space

We show the deviation for Patlak-Keller-Segel system in one-dimensional Euclidean space (Fig. 7A), FitzHugh-Nagumo system in two-dimensional Euclidean space (Fig. 7B), and Barkley system in three-dimensional Euclidean space (Fig. 7C).

We report the MSE for each case shown in Fig. 7, using MSE_{Ψ_i} to denote the MSE of the field Ψ_i that is compared between the “true” and “spatially liberated” neural-learned dynamics:

- Fig. 7A1: $\text{MSE}_A = 1.67 \times 10^{-5}$, $\text{MSE}_B = 4.90 \times 10^{-6}$.
- Fig. 7A2: $\text{MSE}_A = 8.56 \times 10^{-6}$, $\text{MSE}_B = 7.76 \times 10^{-5}$.
- Fig. 7A3: $\text{MSE}_A = 1.24 \times 10^{-5}$, $\text{MSE}_B = 7.98 \times 10^{-5}$.
- Fig. 7B1: $\text{MSE}_V = 2.01 \times 10^{-3}$, $\text{MSE}_W = 1.20 \times 10^{-5}$.
- Fig. 7B2: $\text{MSE}_V = 1.62 \times 10^{-2}$, $\text{MSE}_W = 1.49 \times 10^{-4}$.
- Fig. 7B3: $\text{MSE}_V = 3.03 \times 10^{-2}$, $\text{MSE}_W = 9.16 \times 10^{-4}$.
- Fig. 7B4: $\text{MSE}_V = 4.67 \times 10^{-2}$, $\text{MSE}_W = 1.39 \times 10^{-3}$.
- Fig. 7C1: $\text{MSE}_U = 0$, $\text{MSE}_V = 0$ (initial field configurations are identical).
- Fig. 7C2: $\text{MSE}_U = 3.19 \times 10^{-3}$, $\text{MSE}_V = 3.35 \times 10^{-4}$.
- Fig. 7C3: $\text{MSE}_U = 6.24 \times 10^{-3}$, $\text{MSE}_V = 7.44 \times 10^{-4}$.
- Fig. 7C4: $\text{MSE}_U = 9.31 \times 10^{-3}$, $\text{MSE}_V = 1.15 \times 10^{-3}$.

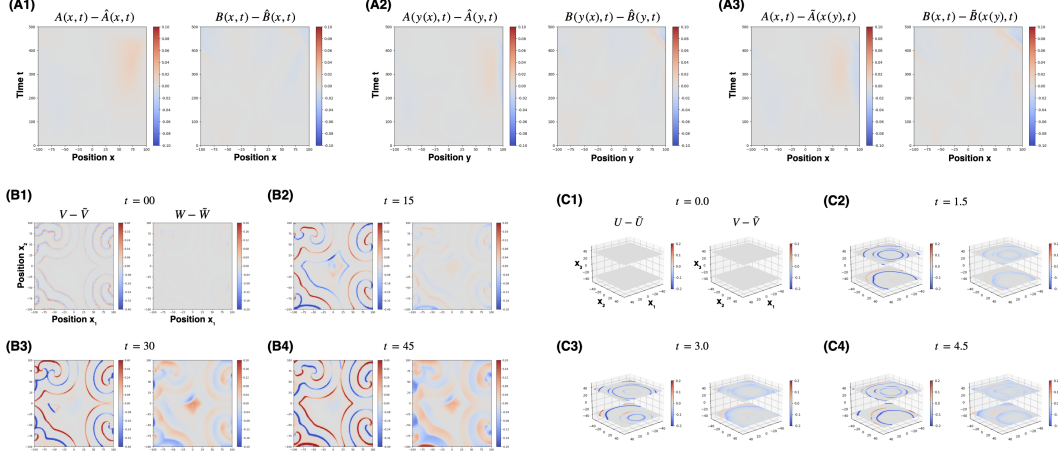


Figure 7: Comparisons between “true” and neural learned dynamics in Euclidean spaces. The deviation range for each field is equal to 10% its dynamical range, with negative deviation colored red-ish and positive deviation colored blue-ish. For Patlak-Keller-Segel system, we show the deviation between Fig. 2B1 and Fig. 2B2 in (A1), between Fig. 2C and Fig. 2D1 in (A2), and between Fig. 2B1 and Fig. 2D2 in (A3). For FitzHugh-Nagumo system, we show the deviation between the top and bottom-rows in Fig. 3A1-4 in (B1-4), respectively. For FitzHugh-Nagumo system, we show the deviation between the top and bottom-rows in Fig. 3B1-4 in (C1-4), respectively. Note that, for brevity, we only label the first plot in (B) and (C), since the rest are identical.

J.2 2-Dimensional Intrinsically curved Surface

We show the deviation for FitzHugh-Nagumo system in two-dimensional curved space, which is embedded in three-dimensional Euclidean space, in Fig. 8.

We report the MSE for each time frame shown in Fig. 8, using MSE_{Ψ_i} to denote the MSE of the field Ψ_i that is compared between the “true” and “spatially liberated” neural-learned dynamics:

- Fig. 8A: $\text{MSE}_V = 5.85 \times 10^{-5}$, $\text{MSE}_W = 1.35 \times 10^{-8}$.
- Fig. 8B: $\text{MSE}_V = 1.36 \times 10^{-3}$, $\text{MSE}_W = 1.51 \times 10^{-5}$.
- Fig. 8C: $\text{MSE}_V = 2.34 \times 10^{-3}$, $\text{MSE}_W = 6.56 \times 10^{-5}$.
- Fig. 8D: $\text{MSE}_V = 4.47 \times 10^{-3}$, $\text{MSE}_W = 1.01 \times 10^{-4}$.

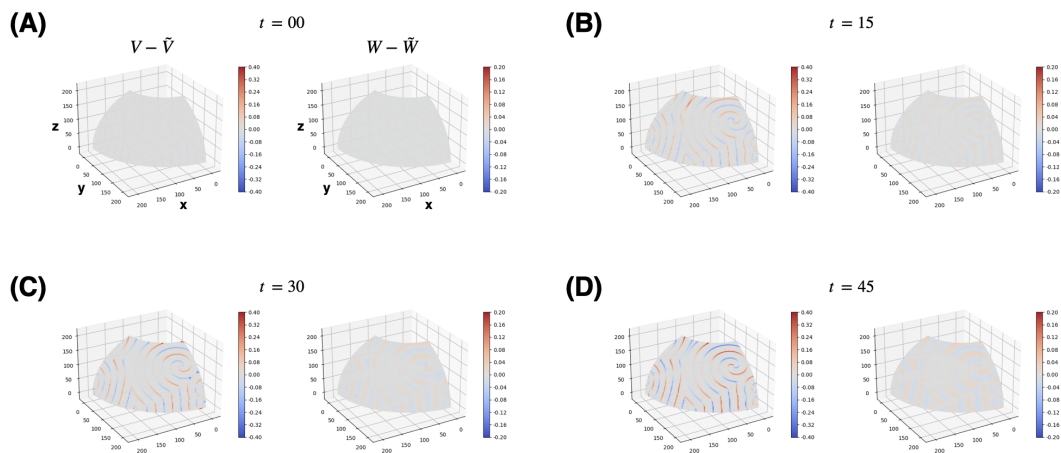


Figure 8: Comparisons between “true” and neural learned dynamics in two-dimensional intrinsically curved surface embedded in three-dimensional Euclidean space. Here we study FitzHugh-Nagumo system, where the deviation range for each field is equal to its dynamical range, with negative deviation colored red-ish and positive deviation colored blue-ish. We show the deviation between the top and bottom rows of Fig. 4D1 in (A), of Fig. 4D2 in (B), of Fig. 4D3 in (C), and of Fig. 4D4 in (D). Note that, for brevity, we only label the first plot, since the rest are identical.